PFC/JA-83-8

ELECTRON CYCLOTRON HEATING IN THE CONSTANCE 2 MIRROR EXPERIMENT

M. E. Mauel

Plasma Fusion Center
Massachusetts Institute of Technology
Cambridge, MA 02139

November 1983

This work was supported by D.O.E. Contract No. DE-AC02-78ET-51013.

PFC/JA-83-8

ELECTRON CYCLOTRON HEATING IN THE CONSTANCE 2 MIRROR EXPERIMENT

M. E. MAUEL
Plasma Fusion Center and
Research Laboratory of Electronics
Massachusetts Institute of Technology
Cambridge, Massachusetts 02139 USA

Abstract—Experimental measurements of electron cyclotron resonance heating (ECRH) of a highly-ionized plasma in mirror geometry is compared to a two-dimensional, time dependent Fokker-Planck simulation. Measurements of the absorption strength of the electrons and of the energy confinement of the ions helped to specify the parameters of the code. The electron energy distribution is measured with an endloss analyzer and a target x-ray detector. These characterize a non-Maxwellian distribution consisting of "passing" ($10eV < T_{e,p} < 30eV$), "warm" ($50eV < T_{e,w} < 300eV$), and "hot" ($1.2keV < T_{e,h} < 4.0keV$) electron populations. The temperature and fractional densities of the warm and hot populations depend upon the absorbed power and the total density. A similar distribution is calculated with the simulation program which reproduces the endloss and x-ray signals. Both the experimental measurements and the simulation are described.

Key words: Electron cyclotron heating, Mirror experiments, Fokker-Planck simulations.

1. Introduction

One of the most successful applications of the quasilinear theory of RF heating has been the modeling of the velocity-space diffusion induced from ion-cyclotron instabilities in mirror-confined plasma[1]. This theory describes the evolution of velocity-space density due to a succession of resonances localized along a particle's bounce orbit. For each pass through resonance, the particle receives a "kick" in its velocity, Δv. The "kicks" result in random motion along specific trajectories in velocity-space provided that the magnitude of Δv is sufficiently large to overlap adjacent bounce resonances[2]. The growth of the ion-cyclotron instabilities—described by a WKB theory—is largely determined by the steepness of the velocity-space gradient at the ion's loss boundary, and this gradient has been self-consistently calculated with use of the bounce-averaged quasilinear equation[3,4].

The WKB/bounce-averaged quasilinear theory is equally well suited to the analysis and design of microwave heating applied at the electron cyclotron frequency. Fundamentally, this requires the generalization of the theory of electrostatic ion-cyclotron heating to include electromagnetic waves, finite parallel index of refraction ($N_{\|}$), and arbitrary polarization.[5,6] Geometric optics is used to determine the wave parameters at resonance, and these parameters are used in a Fokker-Planck simulation to determine the evolution of the electron velocity distribution. The first example of this application was the set of ray-tracing and Fokker-Planck calculations used to predict the steady-state parameters of the ECR heated, TMX-Upgrade experiment[7].

Numerical calculations have also been performed in order to simulate the pulsed electron cyclotron heating of M.I.T.'s Constance 2 mirror experiment.[8] These calculations are unique since (1) the effects of non-zero parallel index of refraction, $N_{\|}$, were included, (2) the code simulated the rapid heating which occurred during the short RF heating pulse ($\tau_{rf} \sim 15\mu sec$), and (3) the code matched the electron and ion loss rates so as to self-consistently calculate the plasma's changing ambipolar potential. The output of the program is the electron distribution function which is then used to calculate the endloss current and the x-ray signals. These are directly

compared to the experimental measurements. The results of the comparison are summarized in this paper and provide experimental evidence supporting the predictions of the electromagnetic quasilinear theory of cyclotron heating of electrons.

This article necessarily deals both with experimental and theoretical aspects of electron cyclotron heating. The first half (Sections 2 and 3) emphasizes the experimental observations and parameters of the heating observed in the Constance 2 experiment while the second half (Sections 4 and 5) emphasizes the theoretical issues pertaining to the numerical simulation of the electron cyclotron heating.

Section 2 describes the Constance 2 experiment and presents relevant results of preliminary investigations which determine (1) the dominant energy loss process of the unheated plasma, (2) the average density and energy of the heated electrons by using the interferometer, diamagnetic loop, and radial probe analysis, and (3) the microwave absorption strength of the electrons. These steps not only introduce the measurements used in Section 3 to characterize the heated electrons but also help to determine parameters used in the simulation. The ion confinement measurements revealed that the ions are cool ($20eV \lesssim T_i < 60eV$) and "flow" through the mirror at the ion thermal speed. This creates a large density at the mirror peaks which in turn allows a large flux of cool electrons to enter the mirror region, lowering the ambipolar potential, and decreasing the warm electron confinement. Radial profiles of the ion saturation current collected by a probe and of the plasma's magnetic field measured by a small magnetic loop determine the radius of the heated electrons. These measurements also indicate large radial temperature gradients—with a relatively cool core and a hotter edge. Finally, by comparing the rate of rise and fall of diamagnetism during ECRH to the input power, the electrons appeared to be strongly absorbing. This is consistent with ray tracing calculations[8,9] performed for the Constance 2 geometry (similar to those reported by Porkolab, *et. al.*[10]) which indicated high parallel index of refraction ($N_{||} \sim 2$) and first pass absorption.

In Section 3, measurements of the warm electron endloss temperature and target x-ray signals are used to characterize the electron energy distribution over the range of densities ($0.1 \times 10^{12} cm^{-3} < \langle n \rangle_{tot} < 10^{12} cm^{-3}$) and energies ($\langle nE \rangle_{tot} < 300 \times 10^{12} eV \cdot cm^{-3}$) studied in the experiment. This is compared to the equivalent "measurements" from the simulation presented in Section 5. The code results and the measurements are similar with the exception that the measured x-ray temperatures are generally a factor of 2 to 4 times larger than that calculated by the program. Uncertainties in the x-ray measurements due to the radial temperature gradients and the axial resonant electric field profile due to strong microwave absorption could account for the discrepancy. Section 5 also compares measured and simulated examples of the time-development of the x-ray and endloss signals. Of particular interest is the time history of the warm endloss current illustrating the

decreased confinement of the magnetically-confined electrons during strong ECRH. The enhanced losses could result from either (1) pitch-angle scattering of the mirror-confined electrons into velocity-space regions strongly-connected by RF diffusion to the loss-cone, or (2) parallel heating due to parametrically excited waves. The first process was predicted by Lichtenberg and Melin[11] and described briefly in terms of the bounce-averaged quasilinear equation in Section 9 of Bernstein and Baxter[5]. This is the "ECRH analog" of the previously mentioned enhanced ion losses induced by ion-cyclotron instabilities. However, the ECRH effect measured and simulated for this paper is much weaker than the ion losses which resulted from direct RF diffusion into the ambipolar hole. Evidence for parallel heating was observed in the absence of cyclotron resonance (*ie.* when the midplane cyclotron frequency, ω_{c0}, was higher than the microwave frequency, ω_{rf}), but it could not be determined whether or not parametrically excited waves accompanied "normal" cyclotron heating (*ie.* when $\omega_{rf} \gtrsim \omega_{c0}$) and contributed to the measured current.[8]

Section 4 describes the use of the bounce-average quasilinear theory in developing the Fokker-Planck simulation. Here it is shown that RF heating induces velocity-space currents with a *direction* determined solely by the microwave frequency and independent of $N_{||}$ and polarization—a fact which greatly simplifies the simulation. An important result of this section is the description of the particle and energy source which represents the flow through the loss boundaries. It is this term which permits a time-dependent calculation. In Section 6, the conclusions from the study are summarized. An appendix is attached describing the numerical techniques used for the simulation.

2. The Constance 2 ECRH Experiment

The Constance 2 experiment was modeled after the earlier Constance 1 and PR-6 experiments[12,13]. The plasma is formed by a plasma gun at one end of a long, two meter guide field. The plasma passes down the guide field and streams through the mirror where a combination of collisional and RF diffusion (induced by injection instabilities) traps some of the ions. By controlling the injection time, the density in the mirror region can be increased beyond $5 \times 10^{12} cm^{-3}$. At the end of the injection, the plasma gun discharge is crow-barred and a fast rise-time divertor coil is energized, isolating the guide-field plasma from the plasma in the mirror-region. Typically, the injection lasts 150 to $400 \mu sec$, and the decay time is between 60 and $120 \mu sec$.

A schematic of the experiment is shown in Figure 1 which illustrates the location of the mirror region, guide field, and the plasma gun. The main mirror and guide-field magnets are outside the vacuum chamber; whereas, the divertor coil and quadrapole stabilizing coils are located within the vacuum chamber. The mirror

ratio is 2:1 and the quadrapoles are energized to produce line-averaged minimum-$|B|$ geometry although most mod-$|B|$ surfaces did not close around the midplane.

Figure 1 also indicates the position of the endloss analyzer, x-ray target, and diamagnetic loop. The endloss detector was the multi-gridded, large-angle acceptance type and was constructed according to the procedures given by Molvik[14]. The analyzer was positioned to examine the core plasma (within 1cm of the axis). To insure that the microwaves would not enter the fan dump region and modify the endloss energy distribution, a stainless-steel screen was placed at the mirror peak (between the plasma and the endloss analyzer) for some of the endloss measurements. The target x-ray detector consisted of four surface barrier detectors (SBD) collimated to look through beryllium filters and operated as described by Petrasso, *et. al.*[15]. Target analysis similar to that reported by Bergston, *et. al.*[16] was required due to the low density of the hot electrons and the short heating times ($\tau_{rf} \sim 15\mu sec$). The differential emission for target x-rays is given by $dI/dE = 10^2 Z(E_0 - E)$, where E is in ergs, Z is the proton number of the target, and E_0 is the energy of the incident electron. The units of the equation are erg/(erg·sterradian) per incident electron. A small (0.63cm) diameter stainless-steel ball supported on a thin (0.2cm diameter) stainless rod was used as the target. The target was placed at the edge of the plasma (about 4cm from the axis) and did not significantly change the overall diamagnetism. One detector was used unfiltered, the remaining three were used with either 1.2, 2.5, or 10.0×10^{-3}cm of beryllium. The detectors have a photon sensitivity below 15keV and above either 0.2keV, 1.0keV, 2.0keV or 4.0keV, depending upon the filter thickness. The ratio of the currents measured with different filters is related to the hot electron temperature by roughly $T_{e,hot} \approx (E_2 - E_2)/ln(I_1/I_2)$, where E_i is the low energy filter threshold and I_i is the current for the ith filter.

In addition to those diagnostics shown, the hot ion temperature was measured with a three-channel charge-exchange analyzer and the density was measured with a 60GHz interferometer. A small magnetic probe was used to estimate the radial extent of the diamagnetic currents, a Langmuir probe measured the radial density profile and the bulk electron temperature, and a floating potential probe was used to measure ion-cyclotron instabilities and monitor the presence of hot electrons. All of the data were digitized, stored, and processed with an interactive, data acquisition system.

Finally, the two primary microwave launch geometries investigated in the experiment and the location of the region lined with the microwave absorbers (Section 2.3) are indicated in Figure 1. The microwaves were generated with a magnetron—pulsed to produce a single, RF burst ($\tau_{rf} \approx 15\mu sec$) during the decay of the plasma. The power was absorbed in the plasma at the resonance surfaces ($\omega_{rf} \sim \omega_{ce}$) which were typically disks on either side of the midplane and generally

extended across the entire diameter of the vacuum chamber. For the experiments reported in this paper, the injected power was between 2 and 20kW. The microwaves were fed into the chamber in either one of two orientations—each directed to the mirror midplane but differing in the angle of the output waveguide to the magnetic field. The launch angles were 10° and 45°, and the open-ended guide was oriented to maximize the coupling of the linearly polarized waveguide mode to the elliptically polarized extra-ordinary mode. The open-ended waveguide illuminated the entire resonance surface.

2.1. The Unheated Plasma

The ions determined the behavior of the unheated plasma. Typically, they were cool and collisional, and the plasma energy and density decayed at a rate proportional to to the ion thermal speed. Three measurements supported this conclusion: (1) the ion endloss temperature indicated $20eV \lesssim T_i < 60eV$, (2) the axial profile of the ion density (as measured with an axially moving Langmuir probe) was flat and unchanging during the decay of the plasma, and (3) the loss rate of the diamagnetism and the line density scaled as the square root of the average energy. The results of the last point are plotted in Figure 2. For mirror-confined ions, the loss rate should scale as the ion-ion collision rate, or $1/\tau_{loss} \sim T^{3/2}/n$. Instead, the ions behave roughly according to a model proposed by Baldwin[17], giving

$$\tau_{i,loss} = \sqrt{\pi}\frac{RL}{V_{i,flow}} + \tau_{ii} log_{10}[R/(1+\phi/T_i)] \qquad (1)$$

whenever ϕ, the difference in the potential from the midplane to the mirror peak, is greater than zero, and

$$\tau_{i,loss} = \left\{\sqrt{\pi}\frac{RL}{V_{i,flow}} + \tau_{ii}[log_{10}(R) + \frac{\phi}{T_i}(\frac{2\phi/T_i - 1}{2\phi/T_i + 1})]\right\} e^{+\phi/T_i} \qquad (2)$$

when $\phi < 0$. $R = 2$ is the mirror ratio, $L = 100cm$ is the distance between mirror peaks, $V_{i,flow} = \sqrt{(T_i+\phi)/m_i}$ is the ion flow velocity, and $\tau_{ii} = 4.5 \times 10^5 T_i^{3/2}/n_i$ is the ion-ion collision time. These equations were used in the simulation to model the ion dynamics.

2.2. The Heated Plasma

A typical shot with microwave heating is shown in Figure 3. From the top of the figure to the bottom, the line density, diamagnetism, and two of the four target x-ray signals are shown for the $500\mu sec$ data record. The solid line represents the average of several consecutive shots and the dots represents the standard deviation. The injection period and RF pulse were $150\mu sec$ and $15\mu sec$, respectively, and these intervals are shown on the graph. The signatures of the ECRH are the large and rapid rise of the diamagnetism, the formation of the hot electrons observed by

the target x-ray detector, and the appearance of "warm" electrons on the endloss distribution. Examples of the endloss distribution—with and without ECRH—are illustrated in Figure 4. These data are generated by rapidly sweeping the electron repeller grid (typically $< 7\mu sec$) , and plotting the collected current versus voltage. Both the increase of the external or "passing" electron temperature (to $\sim 20eV$) and the presence of the warm electrons are shown. These four diagnostics (Figures 3 and 4) constitute the available measurements of the electron energy distribution described in Section 3.

Each shot is characterized by the amount of absorbed power and the average energy and density. The absorbed power is estimated from the rate of rise ($\sim 1/\tau_{rise}$) and the rate of fall ($\sim 1/\tau_{fall}$) of the diamagnetism when the ECRH is turned-off according to the formula

$$P_{abs} \approx \left\langle nT_{\perp} \right\rangle \pi R_p^2 L_p (1/\tau_{rise} + 1/\tau_{fall}) \tag{3}$$

where, in the above, the diamagnetic loop gives $\left\langle nT_{\perp} \right\rangle \pi R_p^2$, and L_p is the effective length of the plasma. L_p was *assumed* to be $60cm$ for the data presented in this article, and the effects of the reduced confinement of the magnetically-confined electrons while the RF is on (described in Section 5) were not included in these estimates. For the case shown in Figure 3, microwave absorbers lined the chamber walls and P_{abs} is about 25% of the incident $25kW$ power. Without the absorbers present, multiple-pass heating occurs and as much as 100% absorption (calculated with Equation 3) is observed.

To determine the average energy and density of the heated electrons, the radius of the plasma and diamagnetic currents were measured with probes. Figure 5 presents these data which illustrate the radial profile of the ion saturation current and the plasma's magnetic field. The magnetic signals are plotted so that diamagnetism is positive and return flux is negative. Examples with and without heating are shown. Without heating, the diamagnetism is due to the ions and the unheated electrons; whereas, with the heating, only the *change* in the magnetic field which results from the ECRH is plotted. Notice that when ECRH is applied, a small rise in density ($\Delta n \sim 0.1 \times 10^{12} cm^{-3}$) is observed at the plasma edge while the radial extent of the diamagnetic currents (as indicated by the shift of the "zero ΔB" radius) doubles. Using $R_p \approx 6cm$, the average density and energy of the example in Figure 3 are $\langle n \rangle \sim 0.3 \times 10^{12} cm^{-3}$ and $\left\langle T_{\perp} \right\rangle \sim 110eV$.

This complicated radial profile of the heated plasma (shown in Figure 4) is emphasized here since it contributes to the uncertainty of the final results. The main diagnostics of the energy distribution are localized measurements. The x-ray target samples the hot edge plasma while the endloss detector maps to the core electrons. The computer simulation, however, calculates only radially averaged quantities (or

more precisely, the distribution along a single field line) and no attempt was made to correct the data for the actual radial profiles.

2.3. Evidence for Strongly Absorbent Plasma.

In general, ECRH absorption is referred to as either strong, "first-pass" heating or weaker, multi-pass or "cavity" heating. During cavity heating, a wide spectrum of $N_{||}$ exists and, if the holes of the cavity are small compared to the area of the resonance surface, the resonant electric field strength increases until the input power is absorbed. On the other hand, for strong first-pass absorption, the $N_{||}$ spectrum is limited and the resonant electric field strength significantly decreases from the vacuum intensity due both to dielectric screening and damping. During strong absorption, the right-handed, resonant electric-field strength is weak near exact resonance and increases rapidly away from resonance and toward the antenna. This tends to preferentially heat those electrons with the largest Doppler-shifted resonance, and, as described in Section 5, this effect was included in the simulation (although in an rather crude way).

For the Constance 2 plasma and for the 10° and 45° end launch geometries, ray tracing predicts $N_{||} \sim 2$ and strong first pass absorption for that fraction of the injected RF which is incident on the plasma ($\sim 50\%$) and couples to the right-handed, elliptically polarized waves ($\sim 50 - 70\%$)[8]. The expected first-pass absorption is roughly 25-35%. With reflecting walls, most of the remaining power is expected to be absorbed through multiple-pass heating.

The experimental measurements are consistent with these predictions and justify the strong absorption assumption which maintains the input power and index of refraction constant while varying the electric field strength. The results of heating are summarized in Figure 6, showing the fraction of absorbed power (as calculated from Equation 3) as a function of magnetic field. Two cases are shown: (1) with "reflecting" walls (*ie.* the aluminium and stainless vacuum chamber), and (2) with "absorbing" walls. For the second case, a thin Urethane-rubber, resonant absorber (Emmerson-Cuming SF-U) lined over 80% of the mirror chamber absorbing greater than 90% of the incident RF. As the magnetic field decreases, the resonant zone moves toward the mirror peaks and the ECRH antennae. The arrows in the bottom figure indicate the axial position of the antenna beyond which little heating is expected.

3. Characterization of the Electron Energy Distribution

Three diagnostics are used to characterize the electron distribution function: (1) the magnitude and decay rate of the diamagnetic signal, (2) the endloss distribution,

and (3) the x-ray signals. The diamagnetic signal in Figure 3, for example, gives an "average" energy of $\sim 110eV$, and its rapid $\sim 15\mu sec$ decay rate demonstrates that most of the observed energy rise is the result of "bulk" heating rather than preferential heating of a very hot electron tail. (For hot electrons, $\tau_{e,hot} \sim 300\mu sec E_{e,hot}^{3/2}$ for a $10^{12}cm^{-3}$ plasma and with $E_{e,hot}$ is units of keV.) The diamagnetic and line density signals are also used to calculate the range of plasma parameters over which the simulation and experiment are compared.

The characteristic warm-electron endloss temperature, the x-ray intensity of the surface barrier detectors are recorded as functions of line density and diamagnetism. These results are plotted in Figure 7 and summarize the characteristics of the non-Maxwellian electron energy distribution observed in this experiment. Each point represents several consecutive shots which were averaged and processed numerically, although each point does not necessarily appear on all four graphs. In particluar, none of the x-ray and endloss measurements were taken simultaneously so that the x-ray target would not perturb the endloss measurement. Notice that for each graph, the data points are labeled according to their magnitudes and *approximate* contours have been drawn to indicate their location on the density-diamagnetism coordinate system. The obvious scatter of each magnitude group is an indication of both shot-to-shot irreproducability and systematic errors during data reduction. The motivation for presenting Figure 7 is that it allows direct comparision to a similar plot calculated by the simulation (Figure 10).

Notice that Figure 7 is divided into four separate contour plots each graphed over the same range of line density and diamagnetism. Assuming that the geometry of the plasma does not vary significantly as the power and line-density changes, these axes are roughly equivalent to the density and absorbed power. Figure 7a shows the variation of the warm endloss temperature observed by sweeping the electron repeller grid in the same manner used to obtain Figure 4. The hottest endloss temperature naturally occurs at the higher powers and lower densities, and the coldest occurs at the opposite extremes. Figure 7b shows the total intensity of the x-ray signal as measured with the unfiltered surface barrier detector. The data indicates a very strong dependence on power and density with a factor of ~ 30 observed between the largest and smallest signal. Finally, Figure 7c and 7d show the ratio of the unfiltered SBD to that with a 0.012mm Be filter ($\sim 1keV$) and the SBD signals with the 0.012mm filter to that with a 0.1mm filter ($\sim 4keV$). If the electrons were Maxwellian, a ratio of 5 would correspond to 450eV and a ratio of 2 would correspond to 900eV. In Figure 7d, a ratio of 2 corresponds to 3.5keV and a ratio of 1.5 corresponds to about 4.0keV.

4. Velocity-Space Currents

4.1. Bounce-Averaged Kinetic Equation

Fundamentally, the Fokker-Planck simulation performed for this study is based on the concept of velocity-space currents. This is a powerful tool in understanding the dynamics of mirror-confined plasma since the open field lines of the mirror create sources or sinks of particles in velocity-space and since the wide range of velocity and cyclotron frequency of the particles as they bounce or pass through the mirror enable large regions of velocity-space to act under the influence of a single wave. If the velocity-space distribution is expressed in terms of the unperturbed orbits of the bouncing or passing particles, then, in the absence of RF or collisions, velocity-space density is constant in time. On the other hand, when the effects of RF or collisions are included, particles "move" in velocity-space with a direction and magnitude defining the total velocity-space current, Γ_v. The fact that RF and collisions can be described by their generated currents merely represents the fact that both processes conserve particles.

Notice that although the total number of particles, N_{tot}, within a mirror region is conserved during RF and collisions, the local density, $n(s)$, is not. Since the orbit of a particle in a mirror depends upon its pitch angle and energy, velocity-space currents generate spatial currents which correspond to changes in $n(s)$. N_{tot} changes only from net particle flow to or from the mirror region to the external plasma.

To model the changes in N_{tot} (and approximately those of $n(s)$), The dynamics of the bounce-averaged distribution (written in this section as $\langle F \rangle$) is derived.[4,5] This is defined in terms of the bounce-time, $\tau_B \equiv \int ds/v_\parallel$, as $\langle F \rangle \equiv \tau_B^{-1} \int dsF/v_\parallel$.

Consider velocity-space represented by a particle's total energy per unit mass ($E = \mu B + \frac{1}{2}v_\parallel^2 + q\phi/m$) and magnetic moment per unit mass ($\mu = \frac{1}{2}v_\perp^2/B$). μ is a constant of the motion, and E is also constant provided the magnetic field, $B(s)$, and potential, $\phi(s)$, are independent of time. s is the coordinate along a field line and $v_\parallel$ and $v_\perp$ are the parallel and perpendicular velocities at s. Furthermore, assume that the mirror is symmetric about so that the distribution, F(v) is independent of the sign of $v_\parallel$. Then, since the Jacobian, $\partial(v_\perp, v_\parallel)/\partial(\mu, E)$ equals $B/v_\perp v_\parallel$, the local density is

$$n(s) = \int \frac{d\mu dEB}{v_\parallel} F(\mu, E, s) \tag{4}$$

and the total number of particles is

$$\begin{aligned} N_{tot} &= A_0 B_0 \int ds n(s)/B(s) \\ &= A_0 B_0 \int d\mu dE \int \frac{ds}{v_\parallel} F(\mu, E, s) = \int d\mu dE \tau_B \langle F \rangle \end{aligned} \tag{5}$$

where A_0B_0 is the magnetic flux through the diameter of the plasma at the midplane, and the order of integration is interchanged allowing integration only over particles accessible at s with $v_\parallel^2 \gtrsim 0$. Now, as seen by Equation 5, if τ_B is independent of time, $dN_{tot}/dt \sim \int d\mu dE \tau_B d\langle F\rangle/dt$, and if $d\langle F\rangle/dt$ is expressed in terms of μ- and E-directed "velocity-space" currents then particle conserving processes are correctly modeled[18].

To calculate these μ- and E-directed currents, the local Boltzman equation is integrated axially. For fixed μ, E, and s, the local equation is

$$\frac{\partial F}{\partial t} = -v_\parallel \frac{\partial F}{\partial s} - \langle \nabla_v \cdot \Gamma_v \rangle \tag{6}$$

where the term in angle brackets ($\langle \ldots \rangle$) is the local divergence of the velocity-space currents, Γ_v, averaged over gyrophase and a volume of space and time small compared to the "microscopic" times and distances of interest but long compared to the applied and thermal fluctuations. Re-writing the divergence in (μ, E)-coordinates by the usual rule for changing variables gives

$$\frac{\partial F}{\partial t} = -v_\parallel \frac{\partial F}{\partial s} - v_\parallel \frac{\partial}{\partial \mu}\frac{1}{v_\parallel}\left\langle \frac{v_\perp \cdot \Gamma_v}{B} \right\rangle - v_\parallel \frac{\partial}{\partial E}\frac{1}{v_\parallel}\langle v \cdot \Gamma_v \rangle \tag{7}$$

Integrating Equation 7 by $\int ds/v_\parallel$ gives the equation for the axially-averaged distribution

$$\frac{\partial}{\partial t}\int \frac{ds}{v_\parallel} F = -\Delta F - \frac{\partial \Gamma_\mu}{\partial \mu} - \frac{\partial \Gamma_e}{\partial E} \tag{8}$$

where

$$\begin{aligned} \Gamma_\mu &= \int \frac{ds}{v_\parallel}\left\langle \frac{v_\perp \cdot \Gamma_v}{B} \right\rangle \\ \Gamma_E &= \int \frac{ds}{v_\parallel}\langle \mathbf{v} \cdot \Gamma_v \rangle \\ \Delta F &= 2[F_+(s = l/2) - F_-(s = l/2)] \end{aligned} \tag{9}$$

To obtain Equation 8, the orbit-average of $F\partial(1/v_\parallel)/\partial t$ at constant (μ, E) was shown to vanish since B and Φ are constant in time.

In Equation 8, ΔF is an important term. It represents the net flux of particles passing into the mirror region from the mirror peaks (at $s = \pm l/2$) and can be considered to be the axial "boundary condition" along each passing orbit resulting from the s-integration. For the trapped particles, ΔF vanishes since the distribution for positive and negative going particles are equal. The factor of two results from the assumption of axial symmetry. This term was also used by Berk and Stewart[3] to calculate the density of passing particles produced from RF-enhanced diffusion into the loss-cone due to ion microinstabilities.

Notice that all of the particles and power which flow into or out of a mirror region are contained in this term. Using Equations 5 and 8, the particle and energy loss rate of the electrons are

$$\frac{\partial N_{tot}}{\partial t} = -A_0 B_0 \int d\mu dE \Delta F \tag{10}$$

$$\frac{\partial \langle E N_{tot} \rangle}{\partial t} = -A_0 B_0 \int d\mu dE \left(E\Delta F - \Gamma_E \right) \tag{11}$$

The terms proportional to ΔF represent the flow of particles or energy to and from the external plasma and provide a means to couple axially adjacent regions. As will be explained in Section 5, the explicit loss terms contained in Equation 10 are essential to the time-dependent calculation of the potential, $\phi(t)$.

Although Equations 8 through 11 correctly describe the averaged electron dynamics, they are not closed. The simulation calculates the dynamics of $\langle F \rangle$ but not $F(s = \pm L/2)$—which is needed to calculate ΔF. An additional approximation is needed which expresses the "outgoing" distribution at $s = \pm L/2$ in terms of the bounce-averaged distribution, $\langle F \rangle$. The "incoming" distribution is assumed to be a Maxwellian of fixed temperature. The bounce-averaged approximation simply implies that the distribution is independent of s along an orbit. But, for the Constance 2 experiment—with cold initial temperatures and rapid ECRH, the bounce-time can be of the same order or longer than the collision or heating times. This permits axial variations of $F(s)$ during transients lasting a few bounce-times. These transients are ignored in the treatment of this paper.

4.2. RF-Induced Velocity-Space Currents

The expression for the RF-induced velocity-space current can be easily derived from the expression for the local current, $\Gamma_{v,rf}$. After expanding in terms of the cyclotron harmonics and averaging over gyrophase, the ith velocity component of the current is

$$\Gamma^i_{v,rf} = -\sum_n \frac{q^2}{m^2} \mathrm{M}^{ij} |E^j E^l| J_n^2 \, Re\{\Omega_n^{-1}\} \mathrm{M}^{lm} \frac{\partial F}{\partial v^m} \tag{12}$$

which is written in the notation used in Mauel[6]. The Lorentz acceleration is $(q/m)\mathrm{M}^{ij}E^j$ with

$$\mathrm{M}^{ij} \equiv \delta^{ij}(1 - \frac{\mathbf{v}}{c} \cdot \mathrm{N}) + N^i \frac{v^j}{c} \tag{13}$$

$\mathrm{N} = \mathrm{k}c/\omega$ is the index of refraction. The argument of the Bessel function, J_n, is $k_\perp \sqrt{2\mu B}/\omega_c$. $Re\{\Omega_n^{-1}\}$ is the real part of the local resonance function[4,5,6]

$$\Omega_n^{-1} \equiv \oint_{-\tau_B \to \infty}^{0} dt' exp(-\int_0^{t'} \nu_n dt'') \tag{14}$$

where ν_n is the Doppler-shifted beat frequency of the RF with the nth harmonic of a particle's cyclotron motion, and it is defined by $\nu_n(t) \equiv \omega - n\omega_c(t) - k_\parallel v_\parallel(t)$. The resonance function represents the dynamics of the wave-particle interaction—the imaginary part representing the reactive energy which "sloshes" between the field and particles, and the real part representing the resistive power transfer. Implied by the definition in Equation 14 was the assumption that (1) $Re\{\Omega_n^{-1}\}$ is sharply peaked at localized resonances (*ie.* when $\nu_n(t) \approx 0$), and (2) the peak interaction is energetic enough that the particles decorrelate with the waves on each successive pass through resonance. If the second condition were not satisfied, lower limit of the orbit integral in the resonance function would have to include several complete bounce periods, resulting in superadiabaticity or bounce-resonance heating. Instead, the contribution of the lower limit can be assumed to be random and ignored.

Equation 12 can be simplified if the velocities are represented by a complex right-handed, left-handed, and $\hat{b}$-directed basis. In this case and after gyro-averaging, $\mathbf{v} = (v_r, v_l, v_\parallel) = (\sqrt{\mu B}\delta_{n,n-1}, \sqrt{\mu B}\delta_{n,n+1}, v_\parallel)$ where $\delta_{n,n\pm1}$ acts to raise or lower the order of one of the Bessel functions shown in Equation. By using the identities below (the last being valid only at resonance),

$$\begin{aligned} v^i \mathrm{M}^{ij} &= v^j \\ N_\perp^i v_\perp^i / c &= (k_\perp \sqrt{2\mu B}/\omega)(\delta_{n,n+1} + \delta_{n,n-1}) = n\omega_c/\omega \end{aligned} \tag{15}$$

it follows that $v_\perp^i \mathrm{M}^{ij} = (n\omega_c/\omega)v^j$ and $v_\parallel^i \mathrm{M}^{ij} = (N_\parallel v_\parallel/c)v^j$. Then, using Equations 9 and 12, the axially-averaged currents become

$$\Gamma^{rf} = -v^i v^j \frac{q^2}{m^2} |E^i E^j| J_n^2 Re\{\Omega_n^{-1}\} \frac{\partial F}{\partial \chi} \tag{16}$$

$$\Gamma_E = \int \frac{ds}{v_\parallel} \Gamma^{rf} \tag{17}$$

$$\Gamma_\mu = \int \frac{ds}{v_\parallel} \frac{1}{B} \frac{n\omega_c}{\omega} \Gamma^{rf} \tag{18}$$

where the operator, $\partial/\partial\chi \equiv (1/B_{res})\partial/\partial\mu + \partial/\partial E$ (for $n \neq 0$) and $\partial/\partial\chi \equiv \partial/\partial E$ (for $n = 0$), defines the RF diffusion paths. Notice that the general quasilinear equation for RF heating in a mirror can be written as a parabolic equation

$$\left.\frac{\partial}{\partial t}\right|_{rf} \int \frac{ds}{v_\parallel} F = \frac{\partial}{\partial \chi} D_{rf} \frac{\partial F}{\partial \chi} \tag{19}$$

where D_{rf} contains information of the RF polarization (through $|E^i E^j|$), index of refraction (N), and wave-particle dynamics (through $Re\{\Omega_n^{-1}\}$), and where the diffusion paths, $\partial/\partial\chi$, depend only upon the harmonic and the wave frequency (and independent of $N_\parallel$). For cyclotron heating (*ie.* $n \neq 0$), the particle's trajectory in velocity-space follows characteristics which correspond to a "kick" in perpendicular velocity ($\Delta v = \Delta v_\perp$) in the local frame where $B = B_{res}$. When $N_\parallel \neq 0$, both

a perpendicular and parallel "kick" is received ($\Delta v = \Delta v_\perp + \Delta v_\parallel$), but, in this case, the resonance is Doppler-shifted by exactly the right amount such that the trajectory is in the same direction as it would have been if $N_\parallel$ had been zero. This has been called longitudinal cooling by Busnardo-Neto, *et. al.*[19] who derived the same conclusion by other arguments. Finally, notice that for waves which Landau damp (*ie.* parallel heating with $n = 0$), $\Gamma_\mu = 0$, reflecting the invariance of μ. Needless to say the simplicity of the diffusion paths greatly simplifies the Fokker-Planck simulation.

The bounce-average contained in Equations 17 and 18 remains to be calculated. Since the diffusion paths, velocities, and electric field, $|E^i E^j|$, have already been expressed by their values at resonance (*ie.* when $\nu(s) = 0$), by already assuming the strong localized resonances, the axial average can be easily estimated by integrating solely over the resonance function, $Re\{\Omega_n^{-1}\}$. These stationary phase integrals have been evaluated[4,5,6] and the result is

$$\int \frac{ds}{v_\parallel} Re\{\Omega_n^{-1}\} = \frac{\pi}{2}\tau_{eff,1}^2 \tag{20}$$

where $\tau_{eff,1}^{-2} \equiv |\nu_n'/2|$. $\nu_n' = -n(d\dot{\omega}_c/ds)v_\parallel - k_\parallel dv_\parallel/dt$ is the derivative of ν_n along a particles orbit, and all quantities are evaluated at $\nu_n(s) = 0$. When the particle turns near resonance or when resonant at the midplane, $\nu_n' \to 0$, and the next order expansion must be used. In this case,

$$\int \frac{ds}{v_\parallel} Re\{\Omega_n^{-1}\} = (2\pi\tau_{eff,2})^2 Ai^2(\nu_n\tau_{eff,2}) \tag{21}$$

where $Ai(x)$ is the Airy function and, in this case, $\tau_{eff,2}^{-3} = \nu_n''/2 = -n(d\omega_c/ds)$ $dv_\parallel/dt - n(d^2\omega_c/ds^2)\,v_\parallel^2 + \omega_b^2 v_\parallel$. The local "bounce-frequency" is defined as $\omega_B^2 \equiv (\partial^2/\partial s^2)\ (\mu B + q\phi/m)$. For computational purposes, the electron orbits were assumed to be elliptical in phase-space ($v_\parallel^2(s) + \omega_B^2 s^2 = v_\parallel^2(s = 0)$), which allowed τ_{eff} to be determined analytically.

4.3. Cyclotron Heating in Constance 2

As explained previously, the validity of the bounce-averaged quasilinear theory places bounds on the strength of the resonant interaction, or equivalently, the diffusion coefficient, D_{rf}. The field must be weak enough to justify the use of the unperturbed orbits during bounce-averaging while large enough to overlap adjacent bounce-resonances. For a typical particle (with $v_{\parallel,res} \neq 0$ and $R_{res} = \omega_{rf}/\omega_{c0} \sim 1.1$), Equation 20 gives the effective interaction time from which follows

$$\frac{\Delta\chi}{\chi} \sim 0.1|E_r|^2(50eV/T_e)^{3/4} \tag{22}$$

where $\chi = E + \mu B_{res}$ and $|E_r|$ is in units of V/cm and T_e in eV. When $v_{\|,res} \to 0$, Equation 21 determines τ_{eff} and $\Delta\chi/\chi$ increases by $(\omega/\omega_B)^{1/6} \sim 4.5$. The bounce-resonance overlap and linearity conditions gives

$$1 \gg \frac{\Delta\chi}{\chi} \gtrsim \frac{\omega_B}{\omega} \sim 10^{-4}(T_e/50eV)^{1/2} \tag{23}$$

For the Constance 2 ECRH experiment, $1.5 < E_r(V/cm) < 20$ so that super-adiabaticity should not be significant for any of the data reported here. On the other hand, the low energy electrons are non-linear. These large, non-linear "kicks" of the low energy electrons are not represented by the quasilinear simulation although it is unlikely that these non-linearities produce serious errors in the final results. This is because the formalism expressed by Equations 7,9, and 10 explicitly conserve particles and energy, and the non-linear currents follow the same trajectories given by equations 17 and 18. In general, error may occur on velocity-space scales finer than $\Delta\chi$ (which for the highest powers and lowest densities equal $\sim 200eV$). However, this requires a strong particle source or sink (which is not expected in Constance) in order to maintain the sharp velocity-space gradients against the "flattening" action of the ECRH.

Finally, it is important to comment on the relative strength of the ECRH diffusion as compared to collisional diffusion. (In the Appendix, Equation A3 shows the collisional currents.) Since Γ_{rf} increases as v^2 and Γ_{col} decreases as v^{-1}, at high velocities, Γ_{rf} can exceed Γ_{col}. In steady-state, $\nabla_v \cdot (\Gamma_{rf} + \Gamma_{col}) \approx \Delta F$, so that when $\Gamma_{rf} \gg \Gamma_{col}$, $\nabla_v \cdot \Gamma_{rf} \approx \Delta F$, and the distribution is approximately determined by the RF characteristics[5]. For RF characteristics which map into the empty passing region, Γ_{rf} represents enhanced losses. For characteristics which map into the filled passing region, Γ_{rf} contributes to RF trapping. In this way, RF changes the spectrum of the loss flux while the variation of the potential insures that the total electron loss rate always equals the ion loss rate.

To estimate Γ_{rf}/Γ_{col}, the μ-directed currents near the loss-boundary are examined. For high velocities ($v \gg v_{th}$), Γ_{col} is dominated by pitch-angle scattering from electrons and ions. Using Equations 9 and A3 and expanding the Rosenbluth potentials in the high-velocity limit (see, for example, Miner, *et. al.*[21]), gives

$$\Gamma_{\mu,col} \approx \int \frac{ds}{v_\| B} v_\perp cos\theta \, \Gamma_{\theta,col} \tag{24}$$

where the pitch-angle current is $\Gamma_\theta = -(1/\tau_{ee})(v_{th}/v)^3 \, \partial F/\partial\theta$ and where $\tau_{ee}^{-1} = 8\pi e^4 \lambda n_e / m_e^2 v_{th}^3$. Equation 24 can be written as

$$\begin{aligned} \Gamma_{\mu,col} &\approx -\int \frac{ds}{B} \frac{1}{\tau_{ee}} (v_{th}/v)^3 \mu v_\| \frac{\partial F}{\partial \mu} \\ &\approx -\frac{L}{B} \frac{1}{\tau_{ee}} (v_{th}/v)^3 \mu v_\| \frac{\partial F}{\partial \mu} \end{aligned} \tag{25}$$

by integrating over a square-well. Equations 16, 18, and 20 give the RF current

$$\begin{aligned}\Gamma_{rf} &= -\mu\frac{q^2}{m^2}|E_r^2|\frac{\partial F}{\partial \chi}\int\frac{ds}{v_\parallel}Re\{\Omega_n^{-1}\} \\ &= -\mu\frac{q^2}{m^2}|E_r^2|\frac{\partial F}{\partial \chi}(\frac{2\pi L_{res}}{\omega v_{\parallel,res}})\end{aligned} \tag{26}$$

where $n=1$, $k_\parallel = 0$, and $(1/\omega)d\omega_c/ds = 1/L_{res}$. If it is further assumed that, near the loss boundary, $\partial F/\partial\chi \approx (1/B_{res})\partial F/\partial\mu$, then the relatively simple formula is obtained

$$\frac{\Gamma_{\mu,rf}}{\Gamma_{\mu,col}} \approx \frac{q^2}{m^2}|E_r^2|\frac{L_{res}}{LR_{res}}\left(\frac{v}{v_{th}}\right)^3\frac{2\pi}{\omega}\frac{1}{v_\parallel v_{\parallel,res}} \tag{27}$$

Notice that for particles near a loss-cone of mirror-ratio, R, $v_\parallel/v = \sqrt{(R-1)/R}$ and $v_{\parallel,res}/v = \sqrt{(R-R_{res})/R}$, simplifying Equation 27 further.

A more useful form of the current ratio can be written by expressing $|E_r^2|$ in terms of the absorbed power, P_{rf}. Using Equation 11,

$$P_{rf} = A_0\int d\mu dE B_0 m_e\,\Gamma_E \tag{28}$$

Assuming that the distribution can be approximated by a Maxwellian ($F(\mu,E) = (4n_e/\sqrt{\pi}v_{th}^3)exp(-2E/v_{th}^2)$) and using Equation 20 throughout the resonance region in velocity-space, permits straight forward integration. The result is

$$P_{rf} = nV\frac{2\pi}{\omega}\frac{L_{res}}{LR_{res}}\frac{q^2}{m}|E_r^2| \tag{29}$$

where $V = A_0 L$ is the plasma volumn. Thus, Equation 27 becomes

$$\frac{\Gamma_{\mu,rf}}{\Gamma_{\mu,col}} \approx \frac{P}{V}\frac{\tau_{ee}}{nT}\frac{1}{4}\frac{v}{v_{th}}\frac{R}{\sqrt{(R-R_{res})(R-1)}} \tag{30}$$

For $R_{res} = 1.2$, $T = 100eV$, $n = 5\times 10^{19}cm^{-3}$, $\Gamma_{\mu,rf}/\Gamma_{\mu,col} \approx (P/17kW)(v/v_{th})$, so that, for the higher power levels typical of Constance 2, endloss enhancements of the warm magnetically-confined electrons by factors greater than two are expected.

5. Numerical Simulation of ECRH

5.1. Brief Description of the Simulation

The time-dependent Fokker-Planck simulation performs three tasks: (1) computes self-consistently the time development of the potential, (2) solves the non-linear second-order partial differential equation for the advancement of the electron

velocity distribution, and (3) diagnoses the distribution to allow comparison with experiment. All three of these tasks are realized by first expressing the distribution function on a spherical grid in velocity-space (*ie.* (v,θ)) and then isolating the particle-conserving velocity-space currents from the axial loss terms. The last step enables numerical calculation of the net loss rate, dn_e/dt, as a function of the time and potential, ϕ, which in trun allows the potential to be advanced in time.

The primary approximation and simplification in the simulation resulted when bounce-averaging the currents in Equation 9. Square magnetic and potential wells represented the actual mirror trap when averaging the collisional currents while for the cyclotron currents parabolic wells were assumed. For both well types, the simple orbits permits closed-form averaging. In addition, in a square-well, $v_{\|}$ is proportional to the longitudinal invariant, $J = \int ds/v_{\|}$ which is conserved as ϕ varies in time. Since $v_{\perp}$ is constant if B doesn't change, the distribution represented on any velocity-space grid is constant in a square-well. The neglect of full bounce-averaging creates errors resulting from the axial variations of $T_e(s)$ and $\phi(s)$. Since the density is roughly constant along the axis, probably the most significant errors electron-electron drag from the hot electrons and RF trapping by ECRH.

Expressing Equation 8 in spherical coordinates gives

$$\frac{\partial}{\partial t}\int \frac{ds}{v_{\|}} F = \Delta F - \frac{1}{v^3}\frac{\partial}{\partial v} v^2 \Gamma_E - \frac{1}{v^2 sin\theta cos\theta}\frac{\partial}{\partial \theta}\{B\Gamma_\mu - sin^2\theta \Gamma_E\} \tag{31}$$

where Γ_e, Γ_μ are given by Equation 9. Then, by bounce-averaging over a square-well,

$$\frac{\partial F}{\partial t} = S + \frac{\Delta F}{\tau_B} - \frac{1}{v^2}\frac{\partial}{\partial v} v^2 \Gamma_v - \frac{1}{v sin\theta}\frac{\partial}{\partial \theta} sin\theta \Gamma_\theta \tag{32}$$

where

$$\Gamma_v = |cos\theta|\frac{\Gamma_E}{L} \tag{33}$$

$$\Gamma_\theta = \frac{1}{L sin\theta}(B\Gamma_\mu - sin^2\theta\Gamma_E) \tag{34}$$

and S represents other explicit sources which for this simulation model the ionization of a fixed background density of hydrogen atoms.

Equation 25 has the required property of a well-defined particle source and sink. Since ionization adds equally to the proton and electron density, the potential is found from the solution to

$$\begin{aligned}\frac{\partial N_{tot}}{\partial t} &= A_0 \int d^3v \Delta F \\ &= -A_0 L(\frac{n_i}{\tau_{i,loss}} - \frac{n_i - n_e}{\Delta t})\end{aligned} \tag{35}$$

with $\tau_{i,loss}$ given by Equations 1 and 2, and Δt equal to the finite time step in the numerical solution. The last term was generally small and was included to control the inevitable numerical errors which result from the finite-difference solution. Notice that both $\tau_{i,loss}$ and ΔF depend upon ϕ.

Having obtained the distribution function, the diagnostics are computed easily. Ignoring transit time effects, the endloss distribution is the current density at the midplane mapped back to endloss analyzer. The endloss distribution is then the integral over the passing region of

$$I(E) = \int_{E+\phi}^{\infty} d^3v v_{\|} F \tag{36}$$

and the target x-ray signals are determined by

$$I_{SBD,i} \sim \int_0^{\infty} dE \sigma_i(E) \int_E^{\infty} d^3v F(v) (\frac{1}{2} m_e v^2 - E) \tag{37}$$

where σ^i is the sensitivity of the detector and filter.

Further details of the numerical procedure are given in the appendix.

5.2. Comparison of simulation with experiment.

An example of the results of the ECRH simulation is shown in Figures 8 and 9. 10kW of RF power with $N_{\|} \sim 2.0$ was applied for 15μsec to a plasma with $n = 0.5 \times 10^{12} cm^{-3}$ and $R_{res} = 1.1$. The temperature of the external plasma was fixed at 15eV, and the external density was set equal to 75% of the midplane density. The ion temperature was 40eV—typical of Constance parameters. Figure 8 shows the computed diamagnetism, potential, resonant electric field strength, and the four target x-ray signals. The average energy increased to 200eV which was stored for the most part in the "warm" electrons making up the majority of the trapped particles. The potential decreased to -4eV with respect to the mirror peaks decreasing the trapping rate of the passing electrons and increasing the loss rate of the trapped electrons. At all times, the total ion and electron loss rates were equal.

The peak electric field strength, $|E_r|$ increased from 7.5V/cm to 9.5V/cm to maintain a constant 10kW absorbed power. This is much lower than the vacuum field strength of 150V/cm due to damping and dielectric screening. The electric field was not constant for all particles. The wave intensity decays as it propagates across the resonant zone, and this effect was roughly modeled by defining $|E_r^2(s)| \sim exp(-(s - s_0)/l)$ where s_0 is the location of the Doppler-shifted resonance of 1keV electrons and $l = 2cm$. This effect tends to heat the hotter particles more than if $E_r(s)$ were uniform. The method is approximate since s_0 and l are unknown.

Figure 9 shows the time-development of the electron distribution. Four contour plots are shown where each contour represents one order of magnitude in velocity-space density. For this example, $R_{res} = 1.1$ and the velocity-space distorts at high

energies along the ECRH diffusion paths. The "effective loss boundary" resulting from characteristics which pass into the loss cone is evident from Figures 9c and 9d.

Nine similar examples were calculated by varying only the initial density and the absorbed power. These spanned three density values and three power values. Contour plots were then drawn which are similar to those drawn to summarize the experimental data for the endloss and x-ray data. Figure 10 shows this plot which can be compared directly to Figure 7.

First, notice that the measured and computed endloss contours are very similar. The major difference occurs at the high powers and low densities where the measured values are found to be slightly higher. The increase in the passing (or external) electron temperature—which was not modeled in the simulation—can account for the difference. A computer run with higher external temperature supports this conclusion.

Examine next Figures 10b and 7b which plot the contours of total x-ray intensity measured from the unfiltered SBD. In the simulation, the x-ray signal is much more sensitive to variations in either the power or density than that measured experimentally. The large discrepancy is believed to be the result of the x-rays emitted from the rod which holds the target as it passes through the lower density edge plasma, instead of any model inaccuracies. This explanation was consistent with floating-probe measurements which indicated denser hot electrons at the edge than in the core during high density discharges.

Figures 10c and 10d show the same two ratios of the SBD's as shown in Figures 7c and 7d. Here, reasonable agreement between the simulated and measured ratios is found although the measured temperatures are as much as a factor of two times hotter than those simulated. The x-rays from the edge plasma may contribute to this error—and undoubtably contributes to the error at high densities. However, at low density, the target is known to be in the region of highest emission so that this "edge effect" can not explain the difference. Instead, the higher experimental temperatures may result from the strong absorption of the microwaves and the high index of refraction. If, for example, the calculation shown in Figure 8 is repeated with $N_{||}$ increased to 4 and the axial position at which $|E_r|$ begins to decay is increased from the 1keV to the 4keV Doppler resonance, then the x-ray temperature doubles and the total intensity increases by a factor of three. The SBD ratios change from 3.8 to 2.1 for the low energy ratio and from 4.5 to 2.3 for the high energy ratio—producing numbers more in line with experimental measurements. This suggests that preferential heating of the hotter electrons due to their greater Doppler-shift may be responsible for the differences in the x-ray ratios calculated and measured.

Finally, since the code is time-dependent, it's interesting to compare the measued and calculated time-behavior of the x-ray and warm endloss signals. Figure 11 shows an example of ECRH heating at 10kW for $n \sim 0.2 \times 10^{12} cm^{-3}$. Both the ratio of the SBDs and the unfiltered intensity are normalized so that the more linear slope of the experimental signal indicates a slower buildup rate than calculated. Especially early in the pulse, the measured temperature was hotter than that calculated.

In Figure 12, the measured (top) and simulated (bottom) warm endloss signals are shown for three density values, 0.2, 0.5, and $1.0 \times 10^{12} cm^{-3}$ at 10kW absorbed power. (The experimental densities were estimated from the line-density and the radial profiles shown in Figure 5.) "Warm" endloss current refers, in this case, to the integral of the current greater than 100eV. The reasons for the fluctuations of the experimental signals were not determined. In this example, the experimental signals rose more quickly than the calculated signals. However, the rapid decrease of the endloss current after the ECRH is switched off is common to both experiment and simulation at low densities and high powers. This rapid decrease (indicated by the small arrow in Figure 12) is evidence of the ECRH enhanced losses described by Lichtenberg and Melin[14]. Since the total endloss must be equal to the ion loss rate, the reduction of the high-energy ($E > 100eV$) endloss corresponds to an increase in the current at lower energies. The "shift" in the endloss spectrum occurs suddenly, as Γ_{rf} vanishes. Other examples were observed experimentally, some with endloss currents during ECRH as much as 4 times larger than that occurring immediately after ECRH. The enhancement was observed to increase with power and R_{res} and decrease rapidly with density[8]. This was the same scaling as given by Equation 30 which was reproduced approximately by the simulation. For example, in the simulation with 20kW and $n_e = 2 \times 10^{11} cm^{-3}$, the ratio of the endloss before the ECRH was switched-off to the endloss 5μsec afterwards was 5. It must be pointed out, however, that it could not be determined that the large enhancement of the endloss was attributed solely to ECRH diffusion. As described in more detail in Mauel[8], parallel heating was observed at high powers and when $R_{res} = \omega_{rf}/\omega_{c0} < 1$, suggesting heating by slow waves, parametrically excited. Parallel heating was distinguished from the usual perpendicular heating by the absence of x-rays and diamagnetism. When $R_{res} > 1$, the parallel heating may persist and contribute to the high endloss with RF, although the degree to which this occurred is unknown. Nevertheless, the fact that the warm endloss current rapidly decreased as the RF was turned off was unmistakable.

6. Concluding Comments

An experimental and numerical analysis of the short, 15μsec, electron cyclotron heating pulse applied to Constance 2 mirror experiment is reported. The confinement

scaling of the ions and the average behavior of the heated electrons were determined in order to correctly formulate the time-dependent Fokker-Planck simulation. The plasma was observed to be strongly absorbing, implying that $N_{\|}$ and P_{rf} are fixed and that $|E_r^2|$ decays from the high magnetic-field regions as the waves propagate into the resonance zone.

The details of the bounce-averaged quasilinear theory were briefly reviewed and the origin of the transit-time source/sink term, ΔF, was derived. This allowed a convenient way to advance the potential numerically.

The major results of the comparison between the experiment and the simulation are summarized in Figures 7 and 10. These contour plots compare the endloss and x-ray signals which make up the available diagnostics of the electron energy distribution. The endloss signal illustrates the cold passing particles and the warm trapped particles, while the target x-rays diagnose the buildup of the hot electrons. Qualitative agreement and some quantitative agreement between the simulation and experiment was observed—especially when reproducing the warm endloss temperature. The most significant disagreement was found between measured and calculated x-ray intensities. This difference probably resulted from errors of the target analysis. The hottest electron temperatures measured in the experiment were as much as a factor of 2 larger than those predicted by the simulation. It is suggested that the preferential heating of electrons with large Doppler-shifted resonances may be responsible for the difference. This explanation is consistent with the observation of strong ECRH absorption.

The time-dependences of the x-ray and endloss signals are also reproduced qualitatively by the simulation. In particular, at low densities and high power, a rapid reduction of the endloss signal is observed when the RF is switched off. This is likely to be the result of the rapid change of the endloss energy spectrum as Γ_{rf} vanishes.

Although reasonable agreement between the experiment and the simulation were found, measurements of the electron energy distribution during the short microwave burst were difficult. The limitations of the target x-ray analysis and the complexity of the radial density and diamagnetic profiles contributed to uncertainty in this comparison. Future Constance experiments have begun which will repeat and expand these measurements for quasi-steady state ECRH discharges. It is hoped that in these experiments a more systematic numerical and experimental comparison will be possible.

Acknowledgments—The results reported here were originally submitted to the Department of Electrical Engineering at M.I.T as a doctoral thesis (Mauel, 1982). The author would like to gratefully acknowledge the his collaboration with his thesis advisor, Professor L. D. Smullin. In addition, R. E. Klinkowstein, J. Irby, and R. Garner collaborated, respectively, with the machine design, axial

density profile measurements, and ray tracing calculations. Ken Retman and Bob Davco helped construct the experimental apparatus. Varian Corporation donated the magnetron used for these experiments. The numerical analysis and the data acquisition system were performed with the use of the MACSYMA Consortium computer supported by United States Energy Research and Development Administration under Contract No. E(11-1)-3070 and NASA Grant No. NSG-1323.

This work was supported by Department of Energy Contract No. DE-AC02-78ET-51013.

Appendix

This appendix describes with more detail the numerical technique used to solve the two-dimensional partial differential equation (Equation 32) given by

$$\frac{\partial F}{\partial t} = S + \frac{\Delta F}{\tau_B} - \frac{1}{v^2}\frac{\partial}{\partial v} v^2 \Gamma_v - \frac{1}{v sin\theta}\frac{\partial}{\partial \theta} sin\theta\, \Gamma_\theta \qquad (A1)$$

The RF-currents are given by Equations 17, 18, 29, and 30, or

$$\begin{aligned} \Gamma_v &= |cos\theta| \frac{\Gamma_E}{L} \\ \Gamma_\theta &= \frac{B}{sin\theta}(1/R_{res} - sin^2\theta)\frac{\Gamma_E}{L} \end{aligned} \qquad (A2)$$

For the collisional currents, the form used by Cutler, *et. al.*[20] is used with

$$\begin{aligned} \Gamma_v &= \Gamma_{e\alpha}(1 - \frac{M_{e\alpha}}{m_e})F\frac{\partial H}{\partial v} - \frac{\Gamma_{e\alpha}}{2}[\frac{\partial^2 G}{\partial v^2}\frac{\partial F}{\partial v} + \frac{1}{v^2}(\frac{\partial^2 G}{\partial v \partial \theta} - \frac{\partial G}{\partial \theta})\frac{\partial F}{\partial \theta}] \\ \Gamma_\theta &= \Gamma_{e\alpha}(1 - \frac{M_{e\alpha}}{m_e})F\frac{1}{v}\frac{\partial H}{\partial \theta} - \frac{\Gamma_{e\alpha}}{2}[\frac{1}{v^2}(\frac{1}{v}\frac{\partial^2 G}{\partial \theta^2} + \frac{\partial G}{\partial v})\frac{\partial F}{\partial \theta} - \frac{1}{v}\frac{\partial^2 G}{\partial v \partial \theta}\frac{\partial F}{\partial v}] \end{aligned} \qquad (A3)$$

where $\Gamma_{e\alpha} = 4\pi e^2 e_\alpha^2 \lambda_{e\alpha}/m_e^2$. H and G are the Rosenbluth potentials which are approximated by a truncated expansion of spherical harmonics.[20] The first seven, even polynomials were used. For electron-ion collisions ($\alpha = i$), G and H were assumed to be spherically symetric and representative of a Maxwellian of a fixed temperature.

Following the remarks made in Miner, *et. al.*[21], Equation A1 is transcribed into a finite-difference equation which represents the dynamics of F on a matrix of cells, $F_{i,j}$, in the (v,θ)-coordinate system. i is the velocity index and j is the θ index. Since the velocity-space currents can always be written as a sum of terms proportional either to F, $\partial F/\partial v$, or $\partial F/\partial \theta$, Equation A3 can be written in the general form

$$\frac{\partial F}{\partial t} = (S + \frac{F_{ext}}{\tau_B}) - \frac{F}{\tau_B} - \frac{1}{v^2 sin\theta}\frac{\partial}{\partial v}(B_1 F + B_2\frac{\partial F}{\partial v} + B_3\frac{\partial F}{\partial \theta}) - \frac{1}{v^2 sin\theta}\frac{\partial}{\partial \theta}(C_1 F + C_2\frac{\partial F}{\partial \theta} + C_3\frac{\partial F}{\partial v}) \quad (A4)$$

with B_i and C_i found in terms of the original v- and θ-directed currents.

The goal of the differencing technique is to explicitly preserve the particle-conserving property of the divergence. This is insured by calculating the current which crosses the boundaries of each cell. Defining $\Gamma_{v,i+1/2,j}$ as the flux which exits the "top" of the (i,j)th cell, and, defining $\Gamma_{\theta,i,j+1/2}$ as the "side", Equation A4 becomes

$$\frac{\partial F_{i,j}}{\partial t} = (S + \frac{F_{ext}}{\tau_b}) - \frac{F}{\tau_B} - \frac{1}{v^2 sin\theta}\frac{(\Gamma_{v,i+1/2,j} - \Gamma_{v,i-1/2,j})}{\Delta v_i} - \frac{1}{v^2 sin\theta}\frac{(\Gamma_{\theta,i,j+1/2} - \Gamma_{\theta,i,j-1/2})}{\Delta\theta} \quad (A5)$$

where

$$\Gamma_{v,i+1/2,j} = \frac{1}{4}(B_{1,i+1,j} + B_{1,i,j})(F_{i+1,j} + F_{i,j}) + \frac{1}{2}(B_{2,i+1,j} + B_{2,i,j})\frac{F_{i+1,j} - F_{i,j}}{\Delta v_+} + \frac{1}{8\Delta\theta}(B_{3,i+1,j} + B_{3,i,j})(F_{i+1,j+1} + F_{i,j+1} - F_{i+1,j-1} - F_{i,j-1})$$

and

$$\Gamma_{\theta,i,j+1/2} = \frac{1}{4}(C_{1,i,j+1} + C_{1,i,j})(F_{i,j+1} + F_{i,j}) + \frac{1}{2}(C_{2,i,j+1} + C_{2,i,j})\frac{F_{i,j+1} - F_{i,j}}{\Delta\theta} + \frac{1}{8\Delta v}(C_{3,i,j+1} + C_{3,i,j})(F_{i+1,j+1} + F_{i+1,j} - F_{i-1,j+1} - F_{i-1,j}) \quad (A6)$$

Δv and $\Delta\theta$ are the widths of the cell, and Δv_+ is equal to $v_{i+1,j} - v_{i,j}$.

Equation A5 is now solved by separating the v- and θ-directed divergences into two tri-diagonal matrix equations which are solved sequentially. These are

$$\delta t A_v F^{t+\delta t/2}_{i-1,j} + (1 + \delta t B_v)F^{t+\delta t/2}_{i,j} + \delta t C_v F^{t+\delta t/2}_{i+1,j} = (F^t_{i,j} + \delta t W_v)$$

$$\delta t A_\theta F^{t+\delta t}_{i-1,j} + (1 + \delta t B_\theta)F^{t+\delta t}_{i,j} + \delta t C_\theta F^{t+\delta t}_{i+1,j} = (F^{t+\delta t/2}_{i,j} + \delta t W_\theta) \quad (38)$$

where

$$A_v = \frac{1}{2v^2\Delta v sin\theta}[(B_{1,i} + B_{1,i-1})/2 - (B_{2,i} + B_{2,i-1})/\Delta v_-]$$

$$B_v = \frac{1}{2\tau_B} + \frac{1}{2v^2\Delta v sin\theta}[(B_{1,i+1} - B_{1,i-1})/2 - (B_{2,i+1} + B_{2,i})/\Delta v_+ - (B_{2,i} + B_{2,i-1})/\Delta v_-]$$

$$C_v = -\frac{1}{2v^2\Delta v sin\theta}[(B_{1,i+1} + B_{1,i})/2 + (B_{2,i+1} + B_{2,i})/\Delta v_+] \tag{39}$$

$$W_v = 0.5(S + F_{ext}/\tau_b) + \frac{B_{3,i+1} + B_{3,i}}{8v^2\Delta v sin\theta\Delta\theta}(F^t_{i+1,j+1} + F^t_{i,j+1} - F^{t+\delta t/2}_{i+1,j-1} - F^{t+\delta t/2}_{i,j-1}) - \frac{B_{3,i} + B_{3,i-1}}{8v^2\Delta v sin\theta\Delta\theta}(F^t_{i,j+1} + F^t_{i-1,j+1} - F^{t+\delta t/2}_{i,j-1} - F^{t+\delta t/2}_{i-1,j-1})$$

Analogous formula are used for A_θ, B_θ, C_θ, and W_θ. At the boundaries (when $v \to 0$ or v_{max}, or when $\theta \to 0$ or $\pi/2$), Γ_v and Γ_θ are zero, and this is reflected easily by modifying the definitions of A, B, C, and W. The tri-diagonal matrix is then inverted, implicitly solving $F_{i,j}(t)$ for each split.

References

[1] D. Baldwin, H. Berk,and L. Pearlstein, *Phys. Rev. Letters* 19, 1051 (1976).

[2] M. Lieberman and A. Lichtenberg, *Plasma Physics* 15, 125 (1973).

[3] H. Berk and J. Stewart, *Physics of Fluids* 20, 1080 (1977).

[4] H. Berk, *Jour. of Plasma Physics* 20, 205 (1978).

[5] I. Bernstein and D. Baxter, *Physics of Fluids* 24, 108 (1981).

[6] M. Mauel, "Theory of Electron Cyclotron Heating in the Constance 2 Mirror Experiment." M.I.T. Research Report, PFC-RR-81/2R, (1981).

[7] B. Stallard, Y. Matsuda, and W. Nevins, *Nuclear Fusion*, 23, 213 (1983).

[8] M. Mauel, ScD Thesis, Dept. of Elect. Eng., M.I.T. (1982).

[9] R. Garner, M. Mauel, and L. Smullin, *Bull. Amer. Phys. Soc.* 26, 893 (1981).

[10] M. Porkolab, *et. al.*, *Nuclear Fusion* 21, 1643 (1981).

[11] A. Lichtenberg, and G. Melin, *Physics of Fluids*, 16 1660 (1973).

[12] R. E. Klinowstein and L. D. Smullin, *Physical Review Letters* 40, 771 (1978).

[13] B. I. Kanaev, *Nuclear Fusion* 19, 347 (1979).

[14] A. W. Molvik, "Large Acceptance Angle Gridded Analyzers in an Axial Magntic Field." LLL Research Report UCRL-52981 (1981).

[15] Petrasso, R., *et. al.*, *Rev. Sci. Instr.* 51 585 (1980).

[16] Begtson, *et. al.*, *Physics of Fluids* 18, 710 (1974).

[17] Baldwin, D. E., "Model for Ion Confinement in a Hot Electron Tandem Mirror Anchor." LLL Report UCID-18802 (1980).

[18] When τ_B changes (due to ϕ changing in time), $J \equiv \int ds v_{\|}$ and μ are conserved and $N_{tot} = \int d\mu dJ \langle F \rangle$. In this case, $d\langle F \rangle/dt$ must be expressed in terms of μ- and J-directed currents. In these coordinates, $\Gamma_J = \int (ds/v_{para})[v_{\|} \cdot \Gamma_v + (1 - \langle B \rangle/B) v_{\perp} \cdot \Gamma_v]$ with $\langle B \rangle = \tau_B^{-1} \int ds B/v_{\|}$. For a square-well, this equation also reduces to Equation 32.

[19] Busnardo-Neto, J., *et. al.*, *Physical Review Letters*, 36 28 (1976).

[20] Cutler, T. A., *et. al.*, "Computation of the Bounce-Average Code", LLL Report UCRL-52233 (1972).

[21] Miner, W. H., N. Winsor, and I. B. Bernstein, *Physics of Fluids* 25 1570 (1982).

Figure Captions

Figure 1. A schematic of the Constance 2 experiment showing the magnets, vacuum chamber, and electron diagnostics (top). The axial magnetic field, potential, and density profiles are those assumed for this analysis.

Figure 2. The ion confinement time measured with the diamagnetic loop. The solid line scales as $1/V_{thi}$. As the density decreases, the plasma confinement begins to increase with V_{thi} along the dotted line.

Figure 3. An example of a typical shot with ECRH heating. The large increase in diamagnetism and hot electron signals as measured with the target x-ray detectors are characteristic.

Figure 4. Examples of the electron endloss signals with and without electron cyclotron heating. Notice (1) the increased "cold" electron temperature from 9ev to 22ev, and (2) the formation of the "warm" endloss current $T_{e,warm} \sim 65ev$. The scales are linear.

Figure 5. The diamagnetic (top) and density (bottom) profiles with and without ECRH heating. With ECRH, the hot edge plasma is indicated by the increased diamagnetism at the edge of the plasma. The increase in plasma density is attributed to ionization and the flow of cold ions from the endwalls.

Figure 6. The ratio of the absorbed power to the injected power with (top) and without (bottom) the microwave absorbing liner. The two curves represent the 10° and 45° launch geometries.

Figure 7. Contours of the warm endloss temperature (a), total x-ray intensity (b), the ratio of the 0.2kev SBD to the 1.0kev SBD (c), and the ratio of the 1.0kev filtered SBD to the 4.0kev SBD signal (d). The scales are the same for all plots—indicating the changing electron parameters as the RF power and total density was changed.

Figure 8. An example of the numerical simulation of the ECRH showing the diamagnetism, potential, electric field intensity, and target x-ray signals. The target x-ray intensities are labeled from "0" to "3" corresponding to 0.5kev to 4.0kev.

Figure 9. An example of the development of the electron velocity distribution during and after ECRH. Shown are four times: (a) at the start of the ECRH, (b) after $5.0\mu sec$, (c) at the end of the $15\mu sec$ RF pulse, and (d) $5.0\mu sec$ after the ECRH was turned off.

Figure 10. Contour plots of the endloss temperature and x-ray signals calculated from the simulation. This plot can be compared to Figure 7. Notice the similarity between the endloss temperatures, and the disagreement in the scaling of the x-ray intensity over the range of densities and powers analyzed.

Figure 11. Actual and simulated x-ray signals verses time during the ECRH pulse.

Figure 12. Measured (a) and simulated (b) time history of the warm endloss current with greater than 100ev. An arrow is placed to indicate the sharp drop in current indicative of the reduction of the ECRH-induced losses.

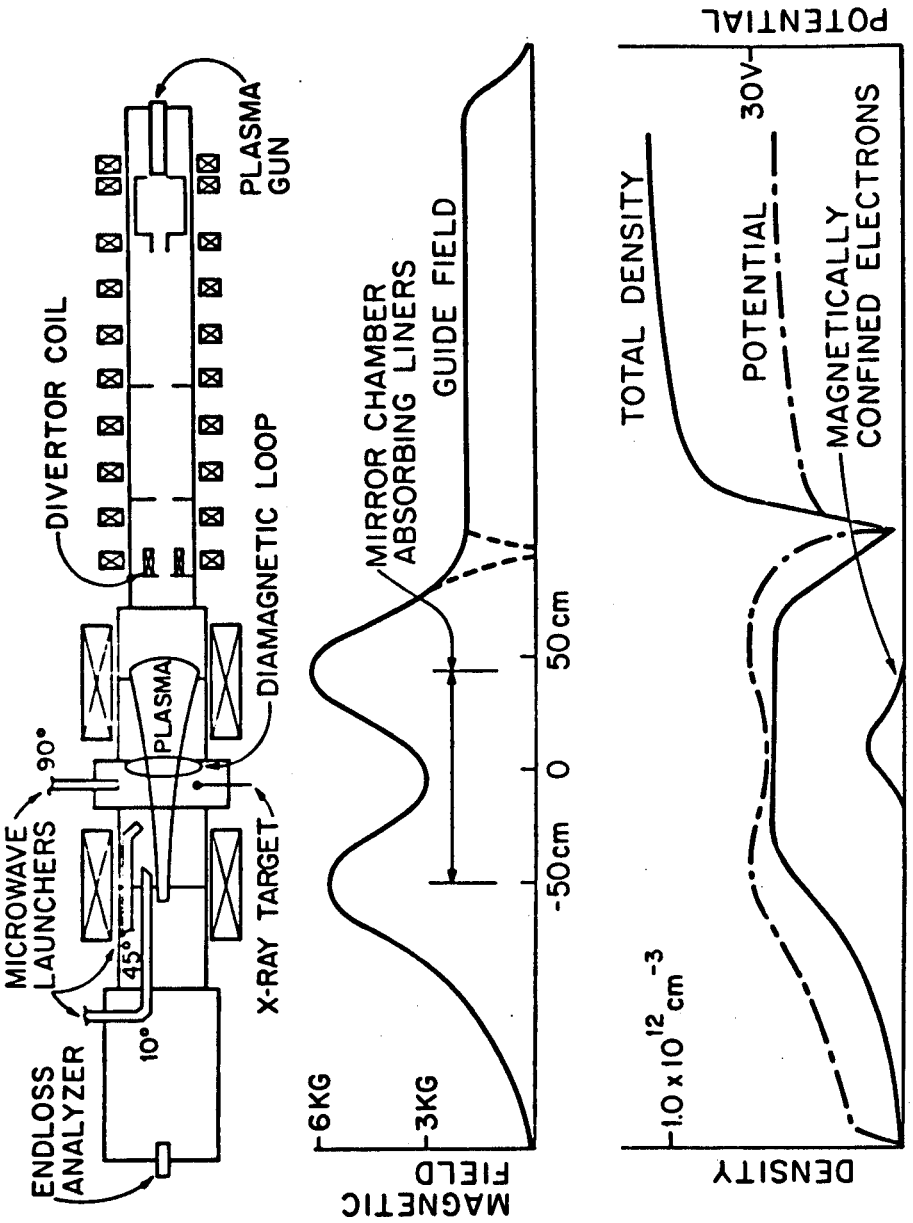
PLASMA GUN
DIVERTOR COIL
DIAMAGNETIC LOOP
PLASMA
90°
MICROWAVE LAUNCHERS
45°
10°
X-RAY TARGET
ENDLOSS ANALYZER
MIRROR CHAMBER ABSORBING LINERS
GUIDE FIELD
50 cm
0
-50cm
6KG
3KG
MAGNETIC FIELD
POTENTIAL
30V
TOTAL DENSITY
POTENTIAL
MAGNETICALLY CONFINED ELECTRONS
1.0 x 10^12 cm^-3
DENSITY

FIGURE 1

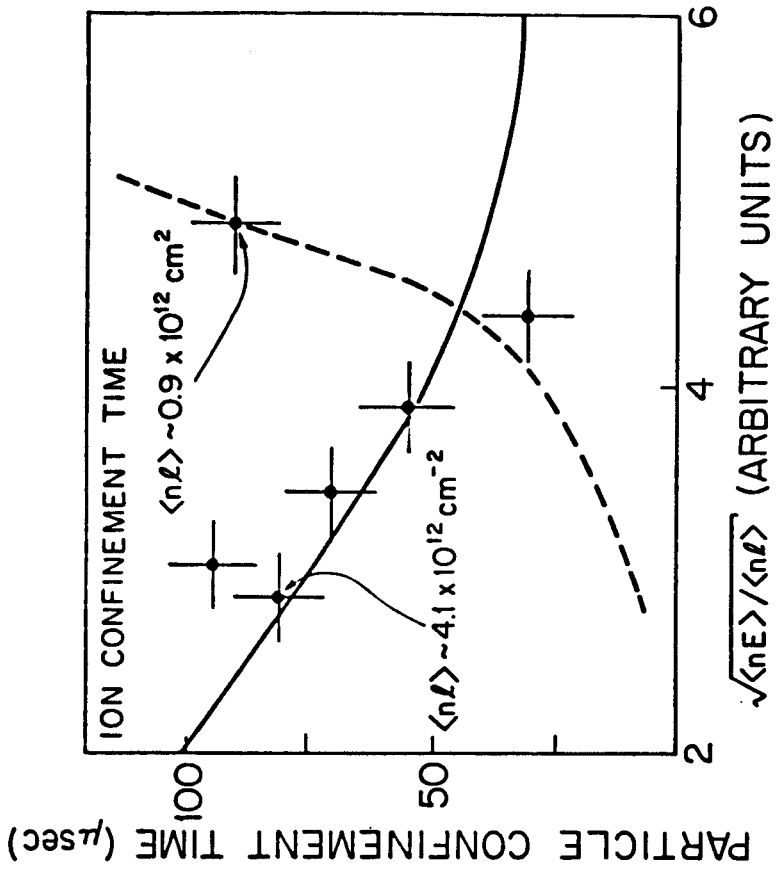
PARTICLE CONFINEMENT TIME (μsec)
100
50
ION CONFINEMENT TIME
⟨nℓ⟩ ~0.9 x 10¹² cm⁻²
⟨nℓ⟩ ~4.1 x 10¹² cm⁻²
2
4
6
√⟨nE⟩/⟨nℓ⟩ (ARBITRARY UNITS)

FIGURE 2

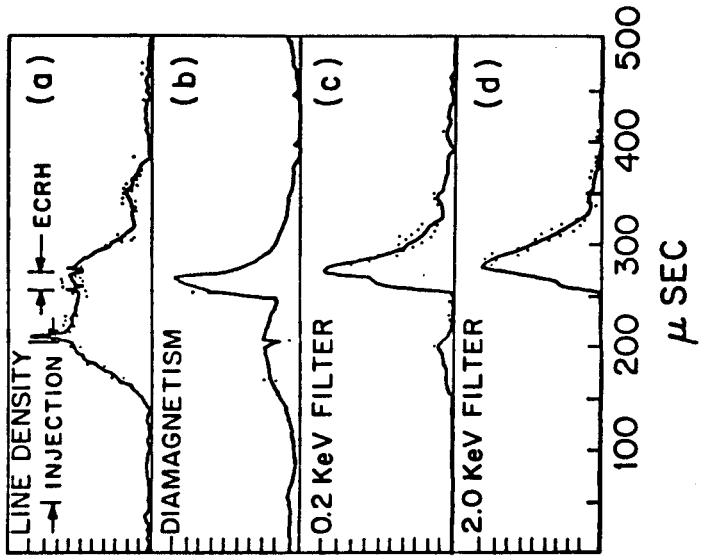
LINE DENSITY
INJECTION
ECRH
(a)
DIAMAGNETISM
(b)
0.2 KeV FILTER
(c)
2.0 KeV FILTER
(d)
100
200
300
400
500
μ SEC

FIGURE 3

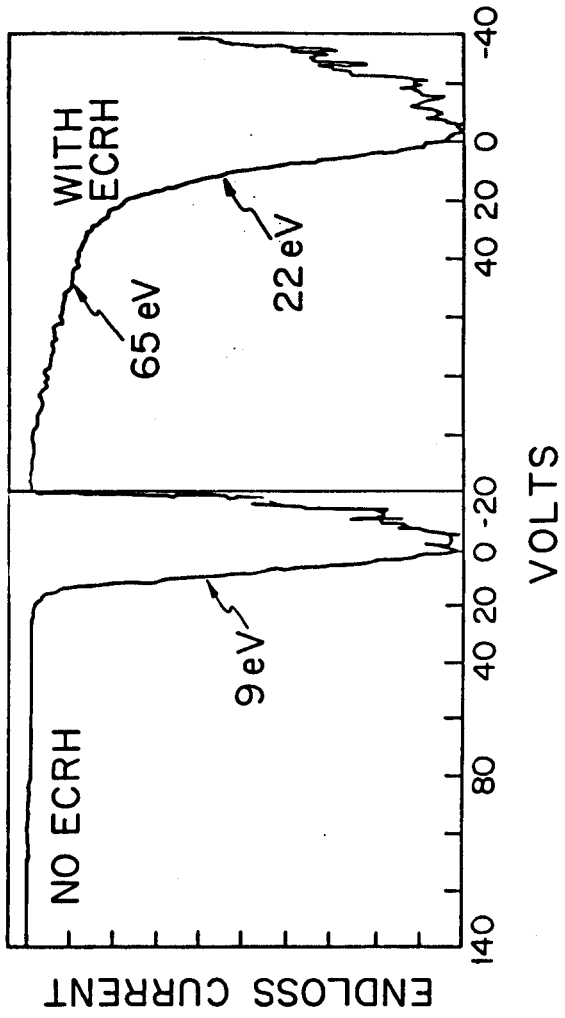
WITH ECRH
65 eV
22 eV
NO ECRH
9 eV
-40
0
40
20
0
-20
40
20
80
140
VOLTS
ENDLOSS CURRENT

FIGURE 4

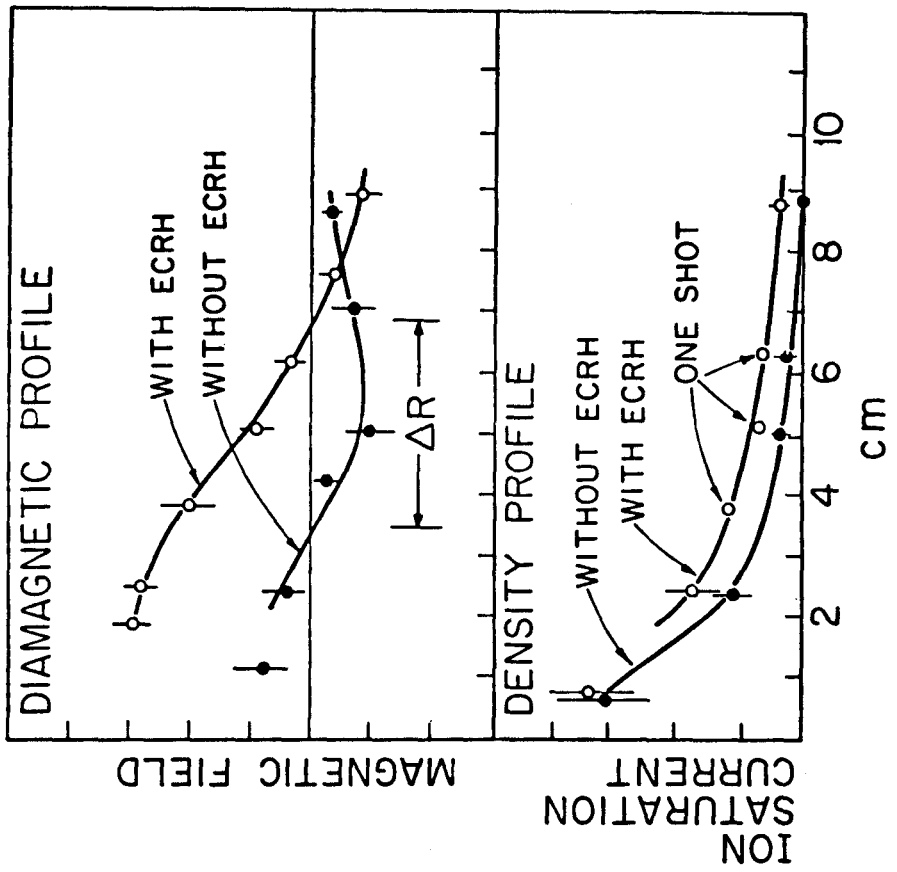
DIAMAGNETIC PROFILE
WITH ECRH
WITHOUT ECRH
ΔR
MAGNETIC FIELD
DENSITY PROFILE
WITHOUT ECRH
WITH ECRH
ONE SHOT
ION SATURATION CURRENT
2
4
6
8
10
cm

Figure 5

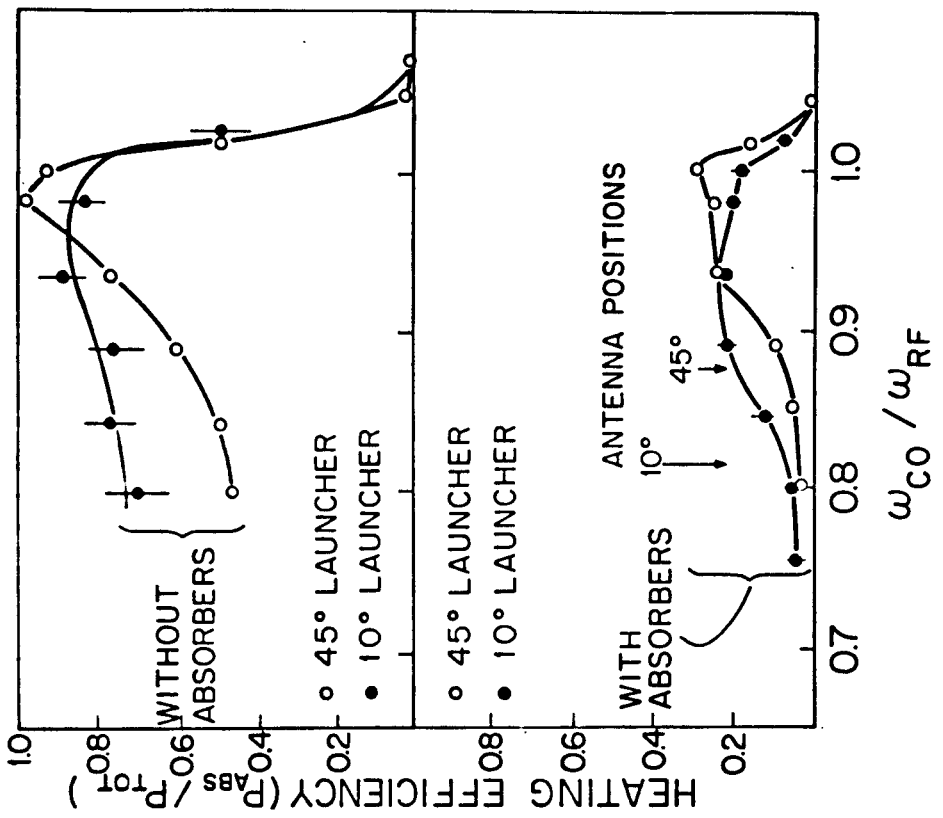
HEATING EFFICIENCY (P_{abs}/P_{tot})
1.0
0.8
0.6
0.4
0.2
WITHOUT ABSORBERS
○ 45° LAUNCHER
● 10° LAUNCHER
○ 45° LAUNCHER
● 10° LAUNCHER
WITH ABSORBERS
ANTENNA POSITIONS
10°
45°
0.7
0.8
0.9
1.0
ω_{CO}/ω_{RF}

Figure 6

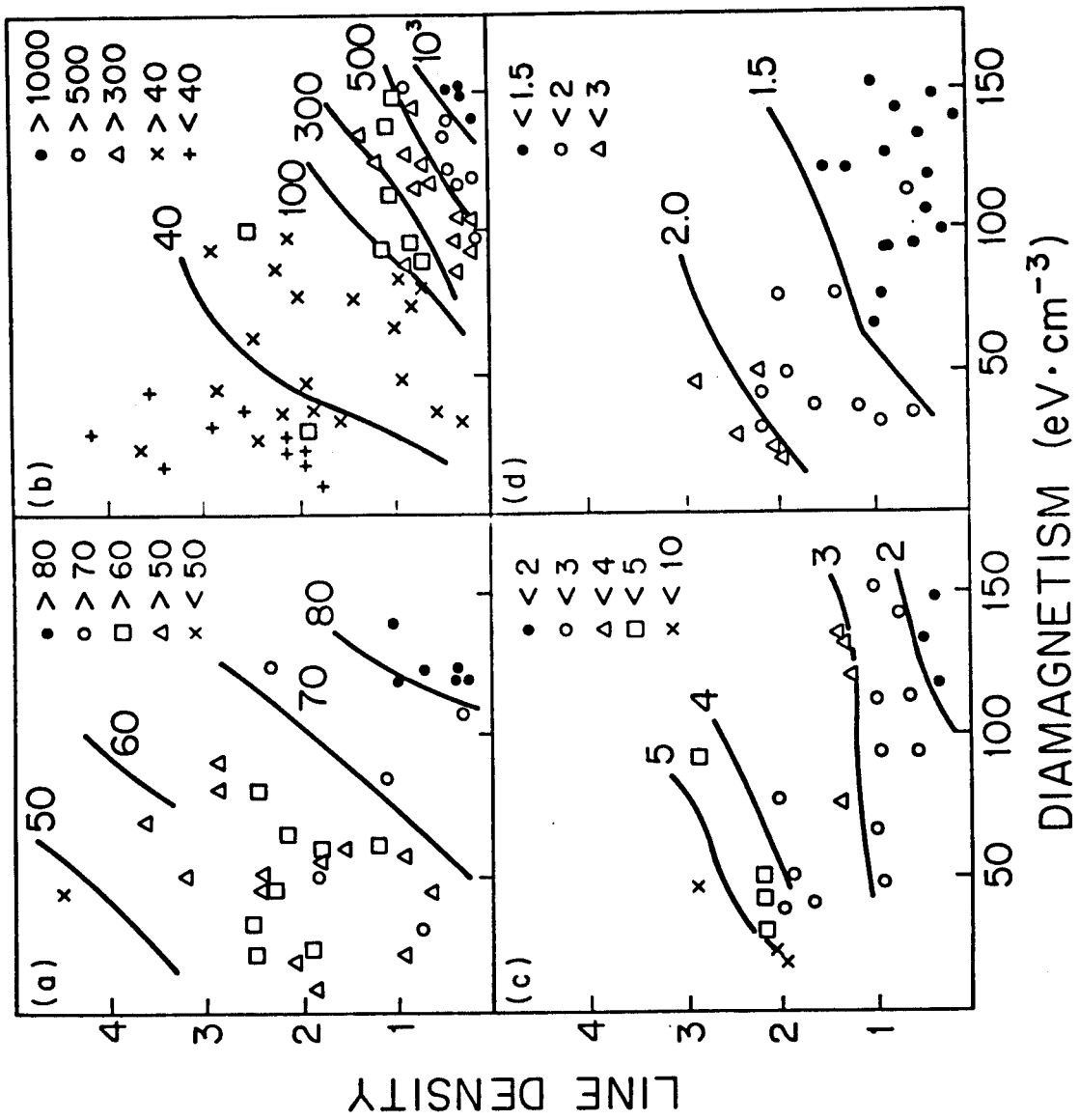
(a)
(b)
(c)
(d)
LINE DENSITY
DIAMAGNETISM (eV·cm⁻³)
> 80
> 70
> 60
> 50
< 50
> 1000
> 500
> 300
> 40
< 40
< 2
< 3
< 4
< 5
< 10
< 1.5
< 2
< 3
50
60
70
80
40
100
300
500
10³
5
4
3
2
2.0
1.5
1
2
3
4
50
100
150

FIGURE 7

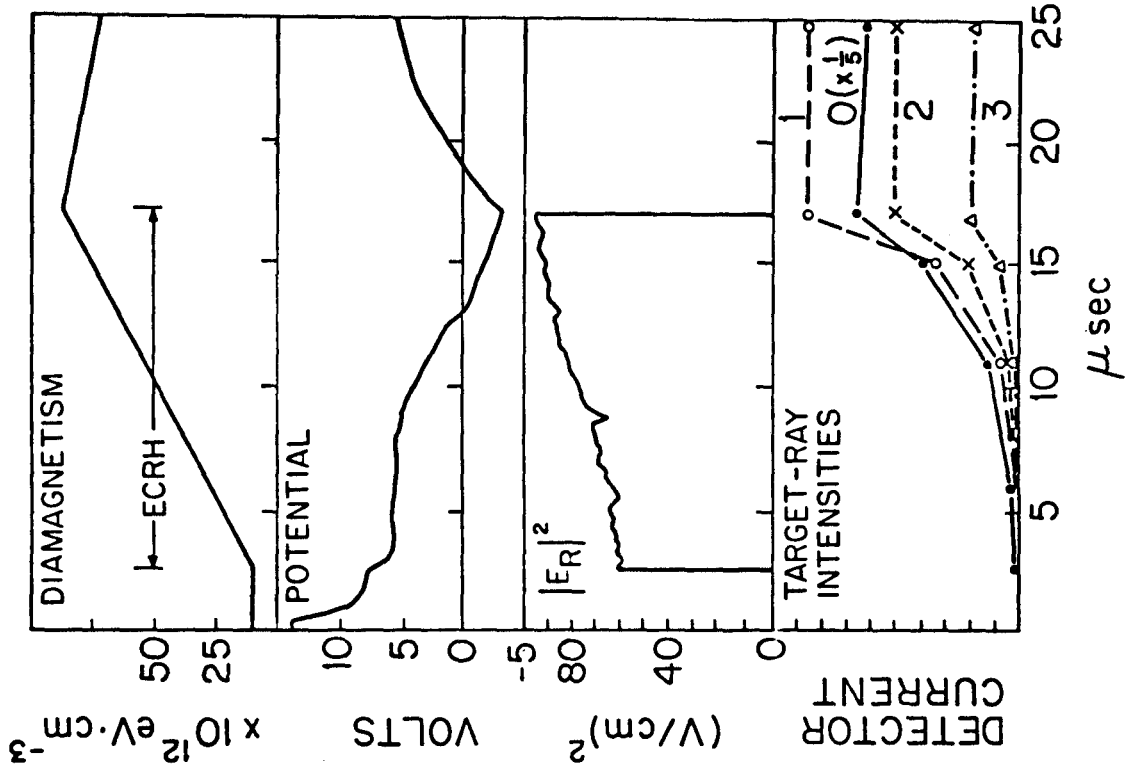
DIAMAGNETISM
ECRH
POTENTIAL
$|E_R|^2$
TARGET-RAY INTENSITIES
O(x⅕)
1
2
3
50
25
10
5
0
-5
80
40
0
5
10
15
20
25
μ sec
x 10^{12} eV·cm^{-3}
VOLTS
(V/cm)^2
DETECTOR CURRENT

Figure 8

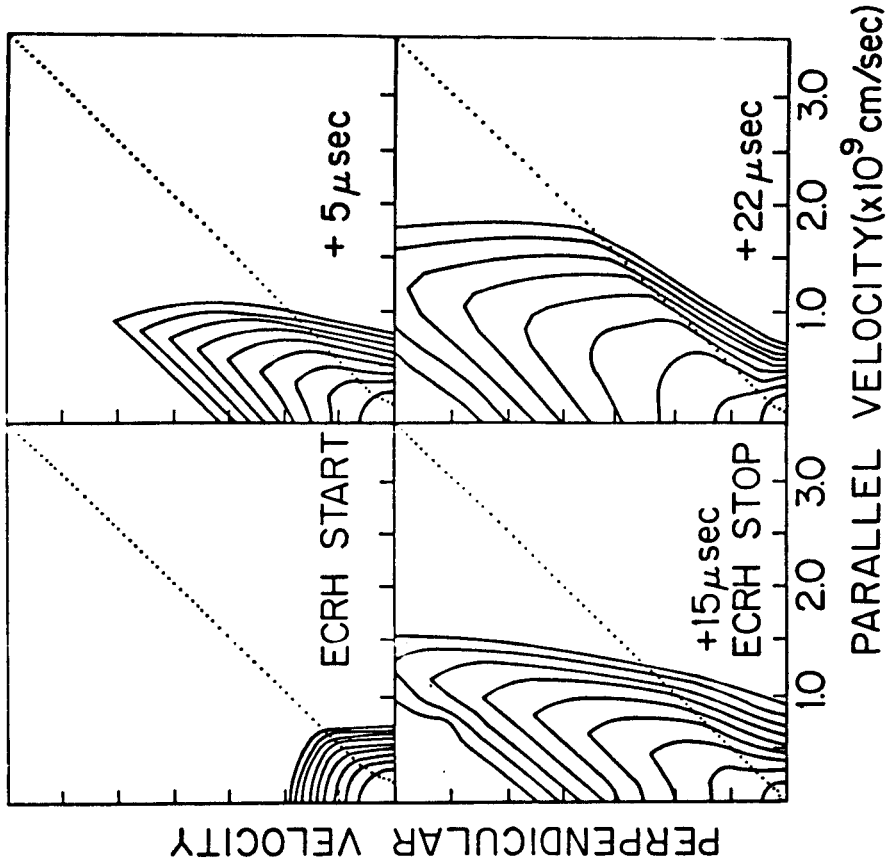
+ 5 μsec
+22 μsec
ECRH START
+15 μsec
ECRH STOP
1.0
2.0
3.0
PARALLEL VELOCITY(x10^9 cm/sec)
PERPENDICULAR VELOCITY

Figure 9

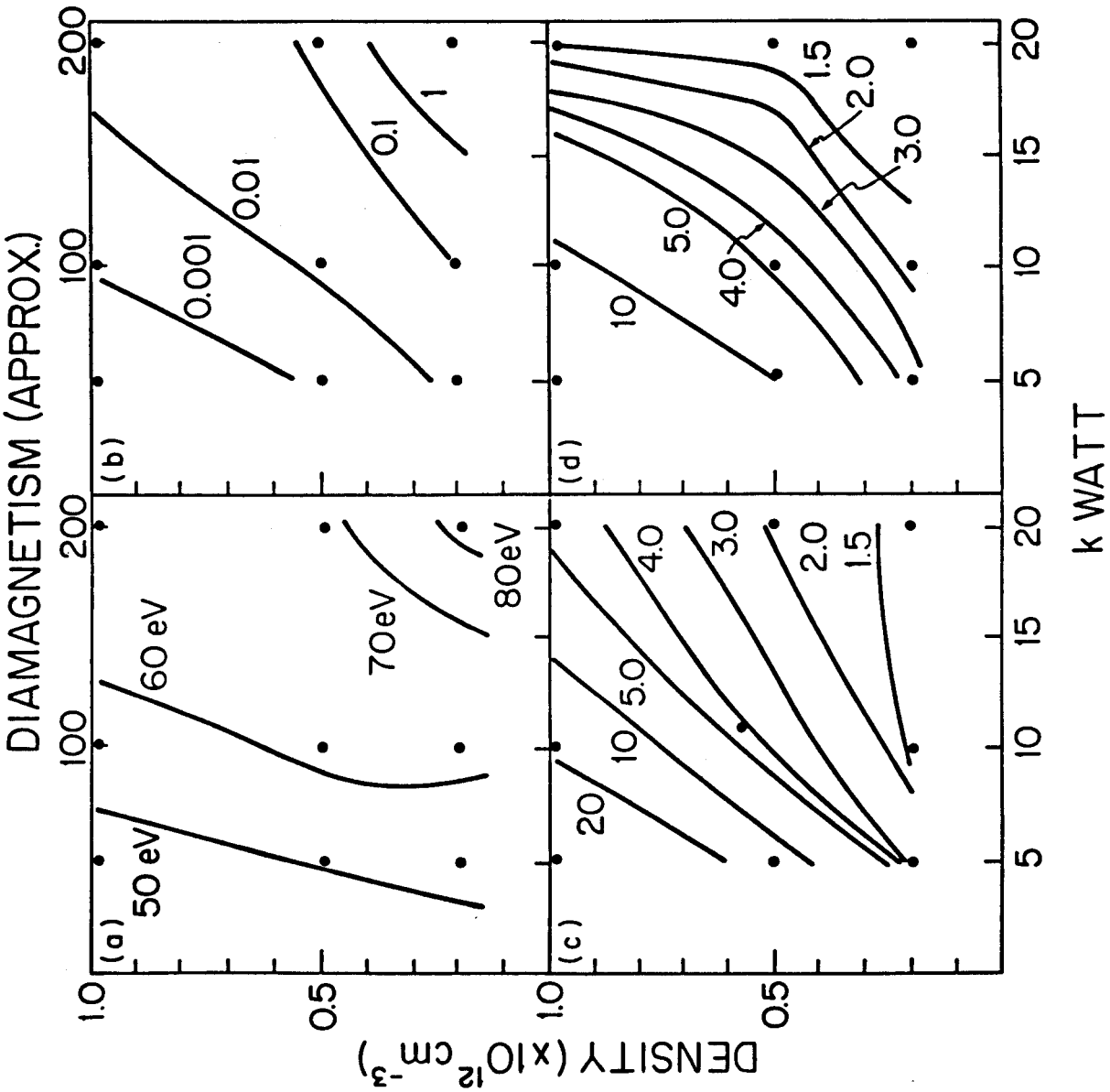
DIAMAGNETISM (APPROX.)
DENSITY (x10^12 cm^-3)
k WATT
(a)
(b)
(c)
(d)
50 eV
60 eV
70eV
80eV
0.001
0.01
0.1
1
10
20
1.5
2.0
3.0
4.0
5.0

FIGURE 10

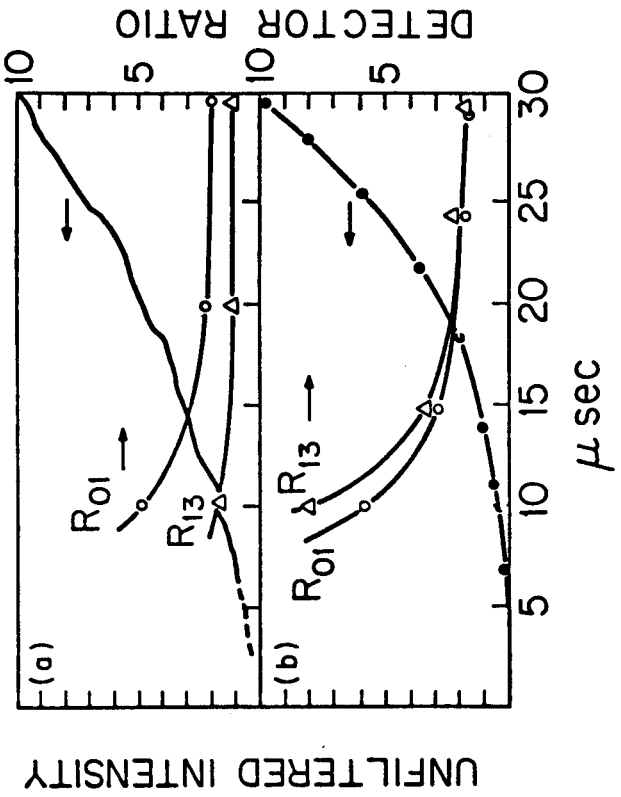
DETECTOR RATIO
10
5
10
5
30
25
20
15
10
5
μsec
R_{01}
R_{13}
R_{13}
R_{01}
(a)
(b)
UNFILTERED INTENSITY

Figure 11

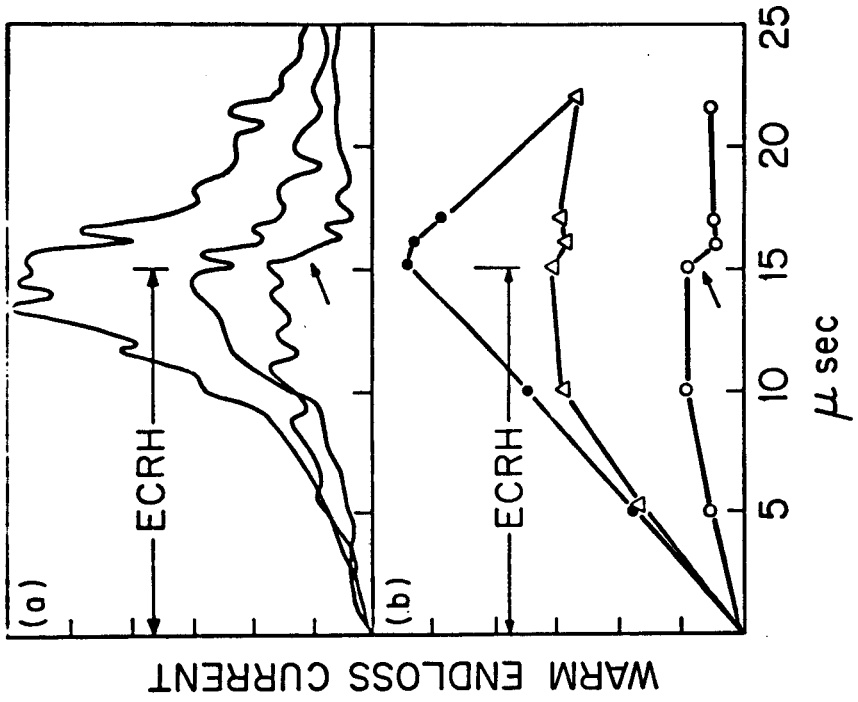

Figure 12